MICROWAVE IMAGING VIA SPACE-TIME BEAMFORMING FOR EARLY DETECTION OF BREAST CANCER: BEAMFORMER DESIGN IN THE FREQUENCY DOMAIN

S. K. Davis, E. J. Bond, X. Li, S. C. Hagness and B. D. Van Veen

Department of Electrical and Computer Engineering
University of Wisconsin
1415 Engineering Drive, Madison, WI 53706, USA

Abstract—Microwave imaging via space-time beamforming has been proposed recently for early-stage breast cancer detection. In this paper we present an efficient frequency-domain approach to designing the beamformers. The low-power signal sequentially transmitted into the breast by each antenna in an array may be either an ultrawideband pulse or a sequence of sinusoidal signals with carrier frequencies corresponding to the discrete design frequencies. Backscattered waveforms collected at each transmitting antenna are processed in the frequency domain using beamformers designed to compensate for frequency-dependent propagation effects in normal breast tissue. Backscattered signal energy is computed and imaged as a function of location. We demonstrate the capability of this method to detect millimeter-sized tumors using representative backscattered waveforms computed from a two-dimensional anatomically realistic FDTD breast model. These simulation results show that localized regions of high energy levels in the images consistently correspond to small malignant tumors present in the breast.

1 Introduction

X-ray mammography remains the preferred method for detecting nonpalpable early-stage breast cancer. Although it provides high-quality images at low radiation doses in the majority of patients, its inherent limitations are well recognized [1]. One alternative technology that is being investigated for breast cancer detection is microwave imaging. The physical basis for microwave detection of breast cancer is the significant contrast in the dielectric properties of normal and malignant breast tissue (see [2]-[5] and the review provided in [6]). The enhanced dielectric properties of breast carcinomas appear to arise in part from increased protein hydration [7] and the contrast is further enhanced by the vascularization of malignant tumors. As a result, malignant tumors have large microwave scattering cross-sections relative to comparably sized heterogeneity in normal breast tissue.

Previous studies investigating microwave imaging for breast tumor detection have proposed tomographic [8]-[11] and ultrawideband (UWB) radar techniques [6, 12],[13]-[15] to exploit the dielectric-properties contrast between malignant and normal breast tissue. Tomographic techniques generally require a large number of transmitting and receiving antennas to be distributed around the object of interest, which complicates the imaging of breast tissue near the chest wall or in the upper outer quadrant of the breast. They also require the solution of a challenging ill-posed nonlinear inverse-scattering problem. UWB radar techniques do not attempt to reconstruct the dielectric-properties profile of the breast, but instead seek to identify the presence and location of significant scatterers, that is, malignant lesions, in the breast from backscattered signals. One UWB radar technique spatially focuses the backscattered signals with a simple delay-and-sum beamformer [6, 14, 15]. The simple delay-and-sum beamformer, however, lacks the capacity to compensate for frequency-dependent propagation effects such as dispersion and cannot optimally discriminate against artifacts and noise.

In this paper, we introduce a frequency-domain design approach for microwave imaging via space-time (MIST) beamforming. MIST beamforming is a signal processing technique that we apply to backscattered waveforms collected by an antenna array placed at or near the surface of the breast. Each element of the array both transmits an UWB pulse into the breast and collects the backscatter, which contains information about the presence and location of malignant tumors that can be extracted by beamforming. The MIST beamformer spatially focuses the backscatter waveforms, compensates for frequency-dependent propagation effects, and optimally discriminates against artifacts and noise. We accomplish these tasks by time-aligning the backscatter, followed by frequency dependent filtering in each antenna channel. The filter frequency responses solve a penalized least squares problem designed to pass signals from a candidate scattering location in the breast with unit gain, subject to soft constraints on the norms of the filters for each channel. MIST beamforming produces a 3-D image of the relative backscatter energy where each pixel of the image represents the energy of the backscatter originating from the corresponding location in the breast. Image locations with high energy implicate the presence of malignant tissue.

The MIST beamformer may also be designed using a time-domain penalized least squares method, as in [12]; however, frequency-domain design leads to a more computationally tractable solution. Given M channels and L filter coefficients per channel, time-domain MIST beamformer design requires inversion of an $ML \times ML$ matrix for each pixel in the design stage. The frequency-domain design, in contrast, circumvents matrix inversions altogether at the cost of selecting multiple penalty weights rather than a single one.

The MIST beamformer for either the time- or frequency-domain designed filters may be implemented in the frequency domain using a series of single frequency measurements to synthesize a broadband input. Assuming M channels and N DFT frequencies, the imaging procedure involves an N-point FFT on the data in each of the M channels, one IFFT plus the matrix multiplication of two $N \times M$ matrices. Thus, the number of computations for each image pixel is on the order of $(M+1)N\log N + 2MN^2$.

The following section of this paper develops our procedure for frequency-domain beamformer design using frequency-dependent propagation models. For ease of presentation we demonstrate our methods in two dimensions (2-D). Section 3 begins with a brief overview of the 2-D computational electromagnetics breast model used to generate representative backscattered signals. It continues with a description

of a 2-D frequency-domain MIST beamformer design and concludes with a presentation and discussion of the resulting images.

Lower and upper case boldface Roman type is used to denote vector and matrix quantities, respectively. Superscript $*$ represents the complex conjugate and superscripts T, H, and -1 represent matrix transpose, complex conjugate transpose, and inverse, respectively.

2 Frequency-Domain MIST Beamformer Design Procedure

For simplicity we consider the monostatic case which is a single-transmit, single-receive configuration[1]. In the monostatic case each antenna, in turn, transmits a pulse into the breast and collects the resulting backscatter before the next antenna repeats the sequence. The collected signals are converted to sampled waveforms containing contributions from the skin-breast interface, clutter due to heterogeneity in the breast, backscatter from possible lesions, and noise. Since the response from the skin-breast interface is much larger than the response from all other contributions, it must be removed prior to performing tumor detection. We accomplish this with the skin-breast artifact removal algorithm presented in [12] which estimates the skin-breast artifact in each channel as a filtered combination of the signal in all other channels. The filter weights are chosen to minimize the residual signal mean-squared error over that portion of the received data dominated by the reflection from the skin-breast interface. This algorithm is shown to effectively eliminate the skin-breast artifact while introducing only a very small level of distortion in the signal backscattered from the lesion.

The image of backscattered energy as a function of scan location $\mathbf{r}$ is obtained by applying a space-time beamformer designed for each scan location to the backscattered signals. Figure 1 illustrates the post-processing performed on the signals for a specific scan location, $\mathbf{r}_0$, following the skin-breast artifact removal. The signals are time aligned, transformed to the frequency domain and pointwise multiplied by the beamformer coefficients. The sum of these weighted signals forms the beamformer output. An inverse DFT transforms the beamformer output back to the time domain where a time-gating window is applied. Finally, the time-gated signal energy is calculated, resulting in the backscatter strength assigned to location $\mathbf{r}_0$ in the image.

[1]Extensions to the single-transmit, multiple-receive configuration are straightforward.

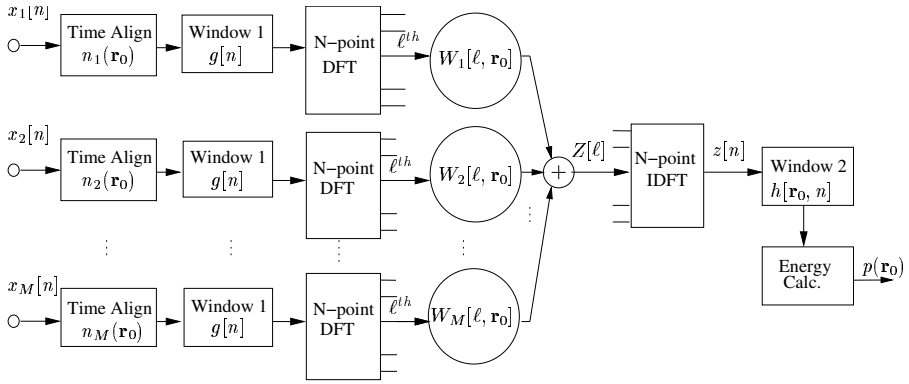

Figure 1: Block diagram illustrating the frequency-domain beamforming process for scan location $\mathbf{r}_0$ in the breast.

For design purposes we assume that the received signal in the i^{th} channel contains only the backscatter due to a lesion at location $\mathbf{r}_0$. Let this received signal after skin-breast artifact removal be denoted by $x_i[n]$ and its DFT denoted

$$X_i[\ell] = I(\omega_\ell) S_{ii}(\mathbf{r}_0, \omega_\ell) \ , \qquad 1 \le i \le M \ , \ 1 \le \ell \le N \tag{1}$$

where ω_ℓ is the frequency corresponding to the ℓ^{th} DFT index, $I(\omega_\ell)$ is the DFT of the transmitted pulse[2] and $S_{ii}(\mathbf{r}_0, \omega_\ell)$ is an analytical model of the monostatic frequency response associated with propagation through breast tissue from the i^{th} antenna to the scatterer located at $\mathbf{r}_0$ and back.

As in [12], we delay the signal $x_i[n]$ by an integer number of samples $n_i(\mathbf{r}_0) = n_a - \tau_i(\mathbf{r}_0)$ so that the waveforms in each channel are approximately aligned in time. Here n_a is the reference sample interval to which all received signals are aligned and $\tau_i(\mathbf{r}_0)$ denotes the round-trip propagation delay for location $\mathbf{r}_0$ in the i^{th} channel in units of sample intervals. The delay is computed by dividing the round-trip path length by the average speed of propagation and rounding to the nearest sample. We choose n_a as the worst case delay over all channels and locations, that is,

$$n_a = \max_{i, \mathbf{r}_0} \tau_i(\mathbf{r}_0) \tag{2}$$

The time-aligned signals are windowed before the filtering stage to remove interference and clutter that is present prior to time n_a using

[2]If a series of narrowband measurements are used in place of a single UWB measurement for each antenna location, then $I(\omega_\ell)$ would represent the amplitude and phase of the ℓ^{th} transmitted sinusoidal signal with carrier frequency ω_ℓ.

the window function

$$g[n] = \begin{cases} 1 & n \geq n_a \\ 0 & \text{otherwise} \end{cases} \tag{3}$$

At this stage the signals are transformed to the frequency domain and passed through the beamformer. The purpose of beamforming is to equalize the transmitted pulse, equalize path-length dependent dispersion and attenuation, interpolate any fractional time delays, and perform spatial discrimination against clutter. The beamformer weight in the i^{th} channel at DFT frequency index ℓ is denoted as $W_i[\ell]$. We design the beamformer using the minimum number of coefficients or equivalently the minimum number of design frequencies. The minimum number of frequency-domain MIST beamformer coefficients, L, may be determined as follows. The maximum distance of any point in the scan region from the antennas determines the time extent of interest for the received signal, and consequently determines the minimum DFT length, N. The DFT length, N, and the sampling frequency, ω_s, determine the spacing between the DFT frequencies as $\Delta\omega = \omega_s/N$. If the bandwidth of interest is B, then the minimum number of frequencies that must be considered in the beamformer design is given by

$$L = \left\lfloor \frac{B}{\Delta\omega} \right\rfloor = \left\lfloor \frac{BN}{\omega_s} \right\rfloor \tag{4}$$

We assume that the band of interest corresponds to the set of L frequencies, $\{\omega_\ell : \ell_0 \leq \ell \leq \ell_0 + L - 1\}$.

In order for the beamformer to compensate for the transmitted pulse and propagation to and from location $\mathbf{r}_0$, we require the output to have unit gain and linear phase as shown by

$$\begin{aligned} & I(\omega_\ell) \sum_{i=1}^{M} S_{ii}(\mathbf{r}_0, \omega_\ell) e^{-j\omega_\ell n_i(\mathbf{r}_0)T_s} W_i^*[\ell] \\ = \; & I(\omega_\ell) \sum_{i=1}^{M} \widetilde{S}_{ii}(\mathbf{r}_0, \omega_\ell) e^{-j\omega_\ell \tau_i(\mathbf{r}_0)T_s} e^{-j\omega_\ell n_i(\mathbf{r}_0)T_s} W_i^*[\ell] \\ = \; & e^{-j\omega_\ell(\tau_0 + n_a)T_s}, \qquad \ell_0 \leq \ell \leq \ell_0 + L - 1 \end{aligned} \tag{5}$$

Here $\widetilde{S}_{ii}(\mathbf{r}_0, \omega_\ell)$ denotes the frequency response due to propagation after removing the linear phase shift associated with round-trip propagation delay, $\tau_i(\mathbf{r}_0)$, the value $\tau_0 = (N-1)/2$ represents the average time delay introduced by the beamformer, and T_s is the sampling interval. Combining the phase factors associated with the propagation and the time alignment according to $n_a = \tau_i(\mathbf{r}_0) + n_i(\mathbf{r}_0)$, we obtain

the design constraints on $W_i[\ell]$ as

$$I(\omega_\ell)\sum_{i=1}^{M}\widetilde{S}_{ii}(\mathbf{r}_0,\omega_\ell)W_i^*[\ell] = e^{-j\omega_\ell\tau_0 T_s}, \qquad \ell_0 \le \ell \le \ell_0 + L - 1 \quad (6)$$

Stack the $W_i[\ell]$ and $\widetilde{S}_{ii}(\mathbf{r}_0,\omega_\ell)$ to form the $M \times 1$ vectors

$$\widetilde{\mathbf{S}}(\mathbf{r}_0,\omega_\ell) = I(\omega_\ell)[\ \widetilde{S}_{11}(\mathbf{r}_0,\omega_\ell)\ \ \widetilde{S}_{22}(\mathbf{r}_0,\omega_\ell)\ \ \cdots\ \ \widetilde{S}_{MM}(\mathbf{r}_0,\omega_\ell)]^T \quad (7)$$

$$\mathbf{W}[\ell] = [\ W_1[\ell]\ \ W_2[\ell]\ \ \cdots\ \ W_M[\ell]]^T \quad (8)$$

and rewrite equation (6) in compact form as

$$\mathbf{W}^H[\ell]\widetilde{\mathbf{S}}(\mathbf{r}_0,\omega_\ell) = e^{-j\omega_\ell\tau_0 T_s} \qquad \ell_0 \le \ell \le \ell_0 + L - 1 \quad (9)$$

If these constraints are satisfied, then the beamformer output at frequency ω_ℓ is given by

$$Z(\omega_\ell) = e^{-j\omega_\ell(\tau_0+n_a)T_s}, \qquad \ell_0 \le \ell \le \ell_0 + L - 1 \quad (10)$$

The beamformer output is converted back to a time-domain signal, $z[n]$, using an inverse DFT and a window, $h[\mathbf{r}_0, n]$, is applied to eliminate additional clutter. The output energy at this scan location, $p(\mathbf{r}_0)$, is obtained from the sum of the squares of the windowed signal

$$p(\mathbf{r}_0) = \sum_n |z[n]h[\mathbf{r}_0, n]|^2 \quad (11)$$

The reconstructed image of microwave scattering strength is obtained by scanning $\mathbf{r}_0$ throughout the reconstruction region and plotting beamformer output energy as a function of location.

The following subsections describe details specific to the design of the filter weights $\mathbf{W}[\ell]$ and the design of the window $h[\mathbf{r}_0, n]$.

2.1 Beamformer Design

Designing the beamformer in the frequency domain has the advantage of yielding an exact solution to (9) which can be expressed in closed-form:

$$\mathbf{W}[\ell] = \frac{\widetilde{\mathbf{S}}(\mathbf{r}_0,\omega_\ell)e^{j\omega_\ell\tau_0 T_s}}{\widetilde{\mathbf{S}}^H(\mathbf{r}_0,\omega_\ell)\widetilde{\mathbf{S}}(\mathbf{r}_0,\omega_\ell)} \quad (12)$$

This solution is especially appealing in comparison to the time-domain approach [12] since it requires no matrix inversion. However, the exact solution is not robust because the magnitude of the beamformer weights can become very large when $\widetilde{\mathbf{S}}^H(\mathbf{r}_0,\omega_\ell)\widetilde{\mathbf{S}}(\mathbf{r}_0,\omega_\ell)$ is small. This

is particularly problematic at higher frequencies and deeper scan locations where attenuation results in small values for $S_{ii}(\mathbf{r}_0, \omega_\ell)$. The robustness of a beamformer to errors between actual and assumed propagation models and to background noise is proportional to the norm of the weight vector [16], [17] or noise gain. Using (12), we have the noise gain

$$\begin{aligned} G_{ls}[\ell] &= \mathbf{W}^H[\ell]\mathbf{W}[\ell] \\ &= \frac{1}{\widetilde{\mathbf{S}}^H(\mathbf{r}_0, \omega_\ell)\widetilde{\mathbf{S}}(\mathbf{r}_0, \omega_\ell)} = \frac{1}{\sum_{j=1}^{M} |\widetilde{S}_{jj}(\mathbf{r}_0, \omega_\ell)|^2} \end{aligned} \tag{13}$$

where the subscript ls refers to the least squares (exact) solution for $\mathbf{W}[\ell]$. Thus, the noise gain of the exact solution can become arbitrarily large as $|\widetilde{S}_{jj}(\mathbf{r}_0, \omega_\ell)|$ decreases.

In order to control the noise gain and obtain a robust beamformer, we consider the penalized least squares problem

$$\mathbf{W}[\ell] = \arg\min_{\mathbf{W}[\ell]} \left[\left| \mathbf{W}^H[\ell]\widetilde{\mathbf{S}}(\mathbf{r}_0, \omega_\ell) - e^{-j\omega_\ell \tau_0 T_s} \right|^2 + \sum_{i=1}^{M} \lambda_i[\ell] |W_i[\ell]|^2 \right] \tag{14}$$

where the first term is the approximation error, the second term is the penalty function, and $\lambda_i[\ell]$, the penalty weight, is selected to trade the norm of $W_i[\ell]$ against the approximation error. Defining $\mathbf{\Lambda}[\ell]$ as an $M \times M$ diagonal matrix with elements $\{\lambda_1[\ell], \lambda_2[\ell], \ldots, \lambda_M[\ell]\}$, the solution to (14) may be written as

$$\mathbf{W}[\ell] = \frac{\mathbf{\Lambda}^{-1}[\ell]\widetilde{\mathbf{S}}(\mathbf{r}_0, \omega_\ell) e^{j\omega_\ell \tau_0 T_s}}{1 + \widetilde{\mathbf{S}}^H(\mathbf{r}_0, \omega_\ell)\mathbf{\Lambda}^{-1}[\ell]\widetilde{\mathbf{S}}(\mathbf{r}_0, \omega_\ell)} \tag{15}$$

Note that as $\lambda_i[\ell]$ decreases the approximation error decreases but the norm of $W_i[\ell]$ increases. In order to compromise between these effects, we select the penalty weights $\lambda_i[\ell] = |\widetilde{S}_{ii}(\mathbf{r}_0, \omega_\ell)|$. With this choice the beamformer coefficients simplify to

$$W_i[\ell] = \frac{\widetilde{S}_{ii}(\mathbf{r}_0, \omega_\ell) e^{j\omega_\ell \tau_0 T_s}}{|\widetilde{S}_{ii}(\mathbf{r}_0, \omega_\ell)| \left(1 + \sum_{j=1}^{M} |\widetilde{S}_{jj}(\mathbf{r}_0, \omega_\ell)|\right)} \tag{16}$$

This solution for the beamformer weights does not require matrix inversion.

We may compare the approximation error and noise gain of this penalized least squares beamformer (16) to those of the unconstrained beamformer in (12). The approximation error of (12) is zero and its

noise gain is given by (13). For the beamformer of (16), the approximation error is given by

$$\begin{aligned} E_{pls}[\ell] &= |\mathbf{W}^H[\ell]\widetilde{\mathbf{S}}(\mathbf{r}_0,\omega_\ell) - e^{-j\omega_\ell\tau_0 T_s}|^2 \\ &= \frac{1}{(1+\sum_{j=1}^{M}|\widetilde{S}_{jj}(\mathbf{r}_0,\omega_\ell)|)^2} \end{aligned} \tag{17}$$

and the noise gain is

$$G_{pls}[\ell] = \mathbf{W}^H[\ell]\mathbf{W}[\ell] = \frac{M}{(1+\sum_{j=1}^{M}|\widetilde{S}_{jj}(\mathbf{r}_0,\omega_\ell)|)^2} = ME_{pls}[\ell] \tag{18}$$

where the subscript pls refers to the penalized least squares solution for $\mathbf{W}[\ell]$. Comparison of (13) and (18) reveals that $\frac{1}{M}G_{pls}[\ell] \leq G_{ls}[\ell]$. Furthermore, (18) indicates that the noise gain of the penalized least squares beamformer cannot exceed M.

2.2 Window Design

If the beamformer satisfies (9) and the lesion is a point scatterer, then the output $z[n]$ is a time-shifted, attenuated and sampled version of a bandlimited impulse. If the values of $Z(\omega_\ell)$ outside the band of interest are set to zero, then $z[n]$ has a sinc function envelope and the majority of backscattered energy is contained within the mainlobe. Since both the time shift and bandwidth are known, the location and width of the mainlobe are also known. If the mainlobe occupies time points n_h through $n_h + \ell_h$ in $z[n]$, then a natural choice for the window is

$$h[\mathbf{r}_0, n] = \begin{cases} 1 & n_h \leq n \leq n_h + \ell_h \\ 0 & \text{otherwise} \end{cases} \tag{19}$$

This choice reduces clutter effects by ensuring that the output energy (11) is calculated using only samples of $z[n]$ containing backscattered lesion energy.

In practice, scattering from the tumor is frequency-dependent, so the beamformer output corresponds to the impulse response of the tumor on the band of interest. These dispersive effects increase the duration of the beamformer output and complicate window selection. Our preliminary investigations suggest that the extent of the increase in duration is directly proportional to the tumor size. Since we are interested in detecting very small lesions, we have chosen to design $h[\mathbf{r}_0, n]$ assuming a point scatterer model. This gives the largest possible signal-to-clutter ratio (S/C) for small tumors. The S/C for larger

tumors is reduced by this choice; however, the backscattered signal from larger tumors is much stronger so a compromised S/C is relatively inconsequential for tumor detection.

3 Results

In this section we demonstrate the effectiveness of 2-D frequency-domain MIST beamformer designs by applying one to FDTD-computed backscattered signals. We begin by describing the realistic numerical breast model used to compute a set of backscattered signals, then we present an example 2-D MIST beamformer design followed by the resulting images and a discussion.

3.1 Computational Electromagnetics Model for Data Acquisition

Representative backscatter waveforms are computed using the finite-difference time-domain (FDTD) method [18]. Our FDTD models simulate the system configuration where a conformal antenna array is placed at the surface of the naturally flattened breast of a patient lying in a supine position. Two-dimensional (2-D) FDTD models of the breast are derived from high-resolution MRI data sets following the procedure presented in [15] for creating realistic numerical breast phantoms.

Variations in the dielectric properties over the frequency band of interest (100 MHz to 20 GHz) are approximated using single-pole Debye dispersion equations with parameters chosen to fit published data on normal and malignant breast tissue [15]. The Debye model for the average complex permittivity of normal breast tissue yields $\varepsilon_r = 9.8$ and $\sigma = 0.4$ S/m at 6 GHz, the spectral peak of the ultra-wideband pulse used in our system. For malignant breast tissue, the Debye model yields $\varepsilon_r = 50.0$ and $\sigma = 7.0$ S/m at 6 GHz. These values result in a 5:1 contrast in permittivity and a 17.5:1 contrast in conductivity. A $\pm 10\%$ variation around the average permittivity and conductivity is employed to model the heterogeneity of normal breast tissue. This variation represents an upper bound on reported breast tissue variability [3, 4]. The high end of this range is assigned to denser fibroglandular tissue while the low end is assigned to less dense adipose tissue. Figure 2 shows an example of an MRI-derived FDTD breast model which illustrates the heterogeneous composition of normal breast tissue. The model includes a 2-mm-thick skin layer ($\varepsilon_r = 36.0$ and $\sigma = 4.0$ S/m at 6 GHz) and a 2-mm-diameter tumor

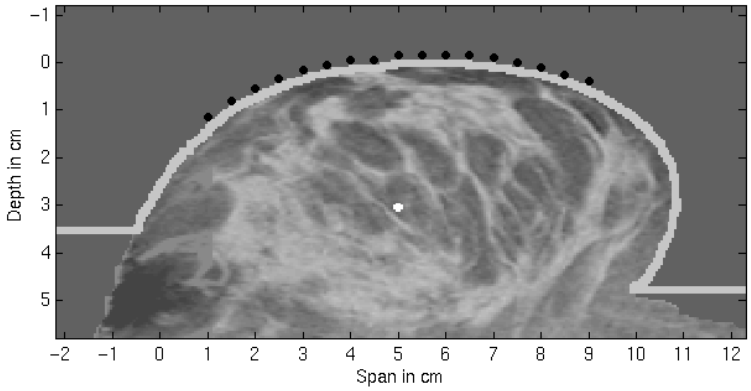

Figure 2: 2-D MRI-derived FDTD breast model containing a 2-mm-diameter malignant lesion at a depth of 3.1 cm. The dots on the surface of the breast represent the positions of the conformal antenna array elements.

artificially introduced at a depth of 3.1 cm below the surface of the skin. A rigid conformal antenna array consisting of 17 elements modeled as electric-current sources is located along the span-axis between 1.0 cm and 9.0 cm on the surface of the breast as indicated by the dots in Figure 2. The antenna array is backed with a synthetic material matching the dielectric properties of skin. The spatial grid resolution is 0.5 mm, and the time step is $\Delta t = 0.834$ ps ($\sim$1200-GHz sampling frequency).

A simulated scan involves exciting each antenna-array element individually with a 110-ps differentiated Gaussian pulse and recording the electric-field response at the same antenna element for approximately 2.5 ns. This process is repeated for each element of the array, resulting in 17 received backscattered signals that contain the scattering contributions from the skin-breast interface (artifact), heterogeneous normal breast tissue (clutter), and the malignant tumor (signal). These sample backscatter signals are processed using our beamforming algorithms to reconstruct a microwave scattering image of the interior of the breast. In order to prepare these signals for processing, we decimate the waveforms from a sampling frequency of 1200 GHz to 50 GHz, the sampling frequency assumed in the design of the beamformer described in Section 3.2.

3.2 Example of a 2-D Space-Time Beamformer Design

In order to illustrate the MIST beamforming algorithm presented in Section 2, we discuss the frequency-domain design of a 2-D space-time beamformer. For ease of presentation we show only the 2-D case, but

these techniques are directly applicable in three-dimensions (3-D).

Frequency-dependent propagation effects are incorporated into the design of the space-time beamformer via a monostatic transfer function, $S_{ii}(\mathbf{r}, \omega)$, which relates the received signal at the i^{th} antenna at location $\mathbf{r}_i$ to the transmitted signal at the i^{th} antenna due to a scatterer located at $\mathbf{r}$. In our 2-D example, we assume that each antenna is an infinite line source of electric current, $I(\omega)$, located at $\mathbf{r}_i$ in a uniform medium of normal breast tissue. The medium's complex wavenumber, $k(\omega)$, is a function of complex permittivity, which is specified using estimates of the average dielectric properties of normal breast tissue. The scatterer is treated as a conducting circular cylinder of radius a and infinite length. For this scenario, we use the following transfer function:

$$S_{ii}(\mathbf{r}, \omega) = \frac{\omega \mu_0}{4} \frac{\left[H_0^{(2)}(k\,|\mathbf{r} - \mathbf{r}_i|)\right]^2}{H_0^{(2)}(ka)}\,, \qquad 1 \le i \le M \tag{20}$$

where $H_0^{(2)}$ is the zero-order Hankel function of the second kind, and the dependence of k on ω is implied. In our present design, we choose $a = 0.1\,\text{mm}$ to approach the regime of a point scatterer, since we are interested in detecting small breast lesions.

The 2-D beamformer is designed for a rigid 1-D conformal antenna array. The array contains 17 elements spanning 8 cm horizontally along the surface of the breast at known locations (illustrated in Figure 2). The 2-D plane that the beamformer is designed to scan spans 10 cm and is 4 cm deep. The transmitted UWB pulse is a differentiated Gaussian with a full width at half maximum equal to 110 ps. Its spectrum has a peak near 6 GHz and significant energy between 1 and 11 GHz.

We design the frequency-domain beamformer over the band 0.5 to 12 GHz and apply a raised cosine taper over the intervals 0.5 to 1 GHz and 11 to 12 GHz to smooth the transition between passband and stopbands. The sampling frequency, f_s, is 50 GHz and the maximum round-trip distance between any antenna and the deepest scan location is 24 cm which corresponds to a time interval of $n_a = 125$ sampling intervals. Thus $N = 125$ is the data record length and $L = 28$ frequencies are employed to span the band of interest. The design location $\mathbf{r}$ is scanned over the breast region using a grid resolution of 1 mm. The post-beamformer window described by (19) is three sampling intervals in length, spanning 60 ps.

Figure 3 illustrates the ideal spatial discrimination capability of this 2-D beamformer. The broadband beamformer gain, defined as

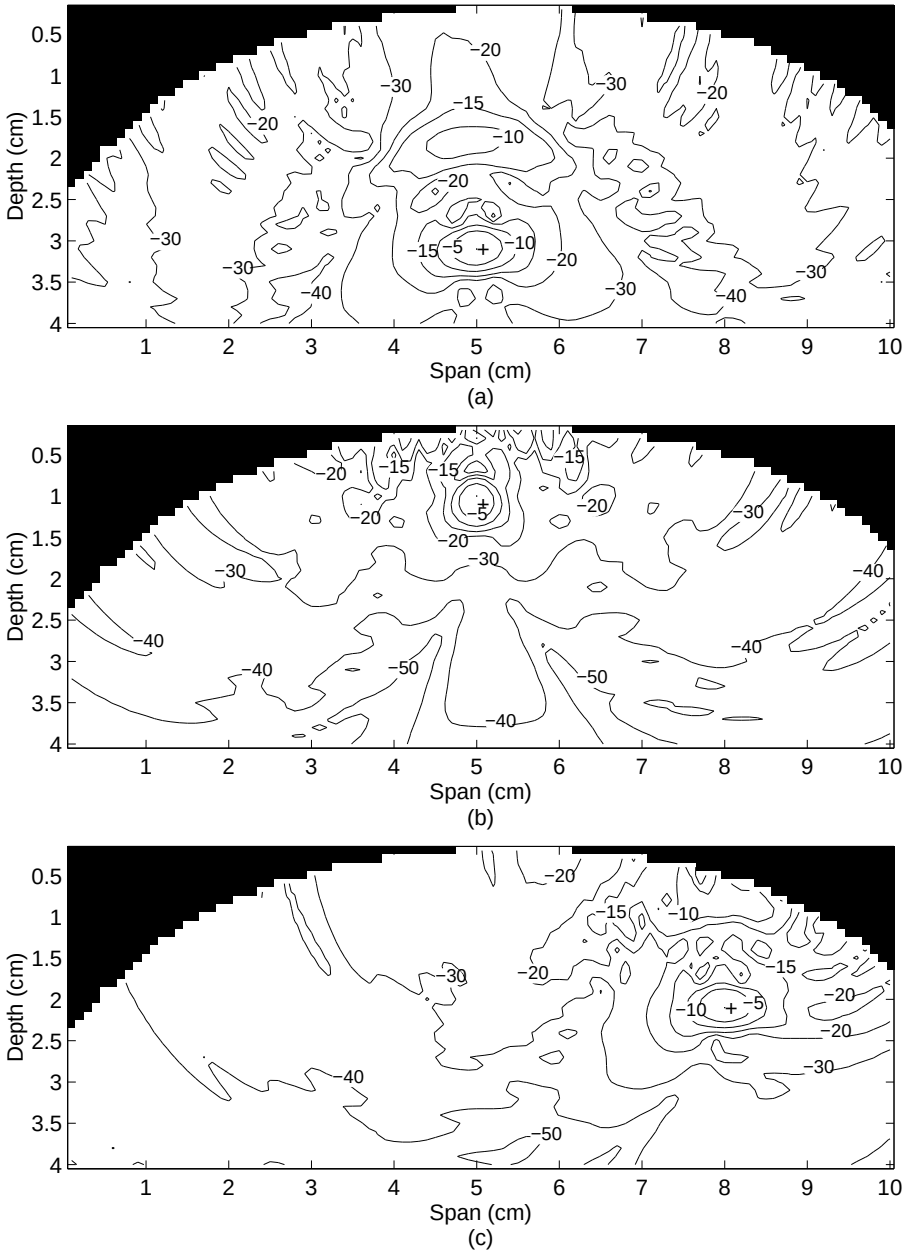

Figure 3: Beamformer gain in dB for a 2-D plane of the breast. The MIST beamformer is steered to the following locations: (a) (5.0 cm, 3.1 cm), (b) (5.0 cm, 1.1 cm), (c) (8.0 cm, 2.1 cm). The first and second coordinates in each pair represents span and depth, respectively. In each pattern, the design location is marked by a '+'.

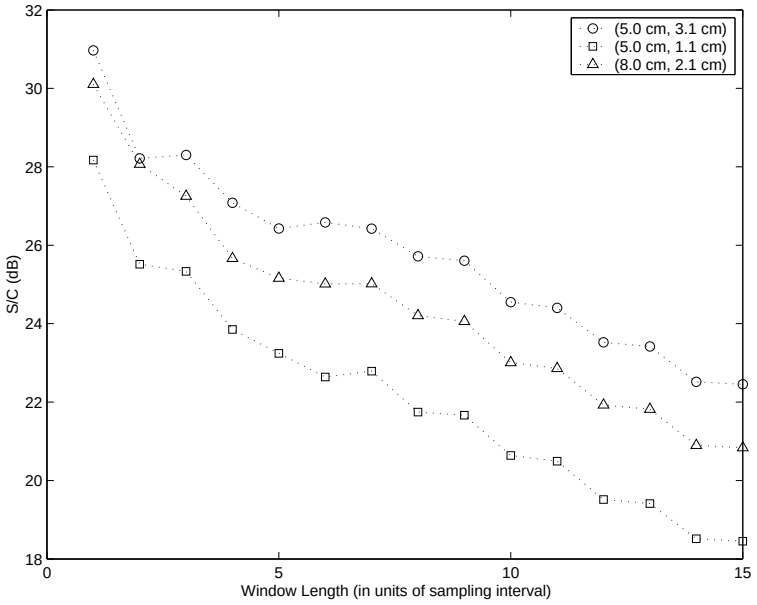

Figure 4: Signal-to-clutter ratios (S/C) for the three example tumor locations as a function of window length.

the output power due to a unit-strength idealized point-scatterer in a homogeneous medium is plotted on a dB scale as a function of scatterer position for three different design locations. Non-idealities such as skin artifacts and heterogeneity of the breast are not modeled in these beam patterns since such non-idealities are patient specific. Although the patterns will deteriorate in the presence of noise and clutter, these patterns are valuable for illustrating the target performance of the beamformer.

In Figure 3(a), the beamformer is designed to pass with unit gain those backscattered signals originating from the location (5.0 cm, 3.1 cm) indicated on the plots by a "+" marker. In Figure 3(b), the design location (5.0 cm, 1.1 cm) is 2.0 cm shallower than that of Figure 3(a). Figure 3(c) shows the gain pattern for a design location (8.0 cm, 2.1 cm) that is off-center with respect to the antenna array. These patterns reveal that the mainlobe of the beamformer decays from 0 dB to -10 dB gain within a 0.5 cm radius of the design location. A strong sidelobe is apparent in each pattern approximately 1.3 cm from the design location on the array side; however, the sidelobe levels are at least 5 dB below the mainlobe.

Figure 4 shows the approximate S/C for three example tumor locations as a function of window length. The signal energy is approximated by steering the beamformer to the center location of a 2-mm-

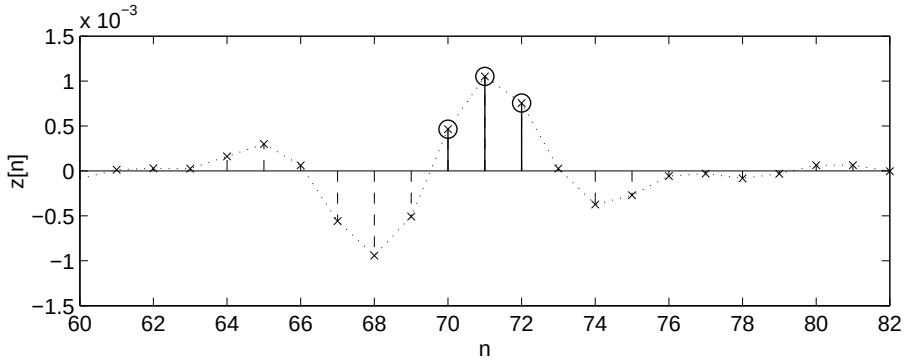

Figure 5: Output signal when the beamformer is steered to center of a 2-mm-diameter malignant tumor similar to the numerical breast phantom of Figure 2. Samples falling within the three-sample rectangular window are signified by a circle surrounding the 'x' of the beamformer output signal. The tumor is centered at (5.0 cm, 3.1 cm).

diameter tumor, applying windows of varying length to the beamformer output, and calculating the output energy. Similarly, the clutter energy is computed by applying the same process to backscatter waveforms obtained from a tumor-free model, repeating for each scan location within the central 6 cm × 2 cm region of the breast, and averaging the results. Although these curves suggest that a one-sample window yields the maximum S/C, we choose a window length of three samples (60 ns) in order to balance the goal of maximizing S/C with the goal of maintaining robustness to dispersion. Figure 5 shows the position of the three-sample window relative to the beamformer output waveform when the beamformer is steered to a malignant tumor at (5.0 cm, 3.1 cm). In this plot, the circled samples fall in the window and all other samples are outside the window. Clearly, a larger window would capture more signal energy at this scan location, but that same window would capture more clutter energy when the beamformer is steered elsewhere in the breast. The goal of preserving signal energy while discriminating against clutter suggests this strategy of optimizing S/C rather than signal energy alone.

3.3 MIST Beamforming Images

Figure 6(a) depicts on a dB scale the scanned beamformer output energy for the breast model of Figure 2, which contains a 2-mm-diameter malignant tumor located at a depth of 3.1 cm. The white "+" sign in the image indicates the location of the center of the modeled tumor. The origin of the dominant energy in this image, localized around

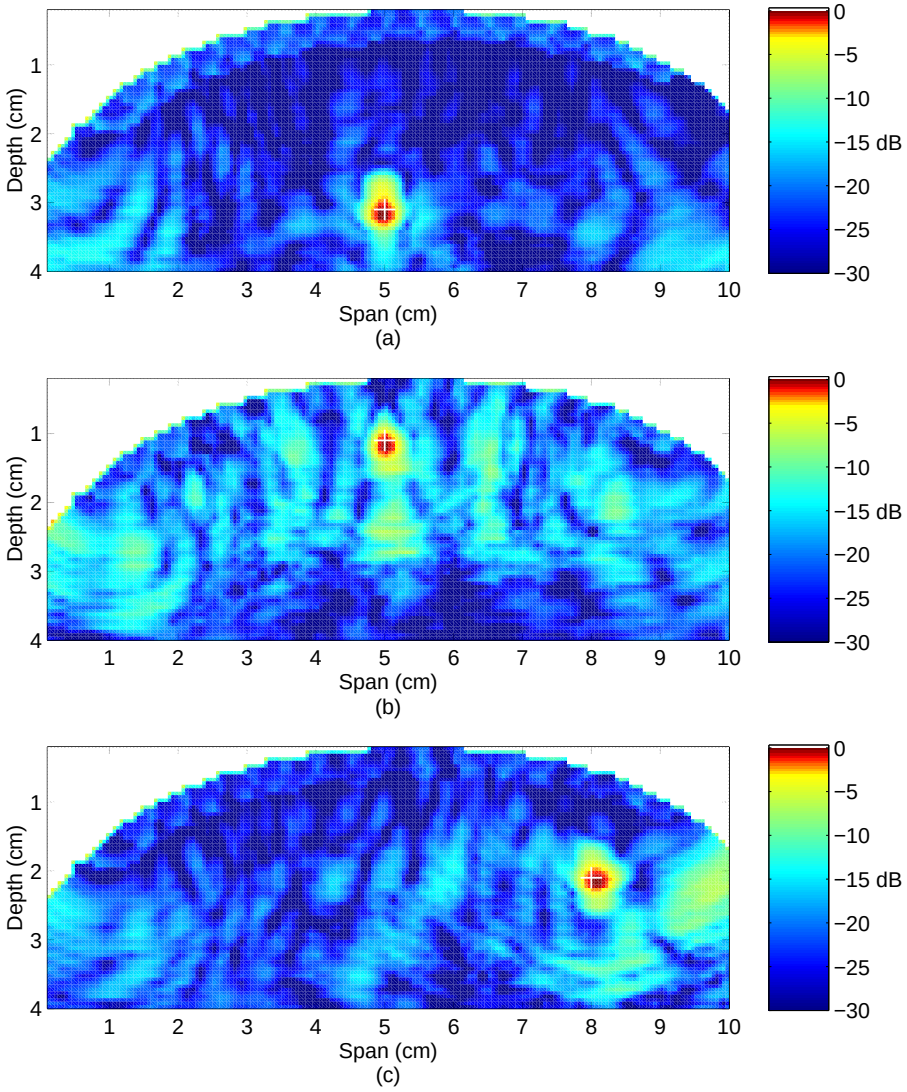

Figure 6: Color images showing the backscattered energy for numerical breast phantoms similar to Figure 2 with a 2-mm-diameter malignant tumor centered at (a) (5.0 cm, 3.1 cm), (b) (5.0 cm, 1.1 cm), (c) (8.0 cm, 2.1 cm).

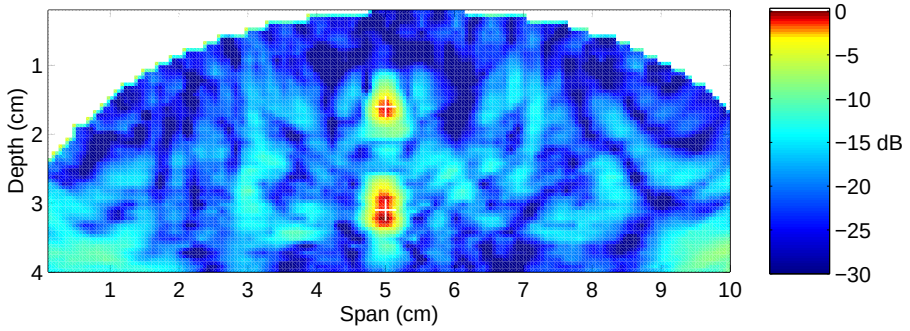

Figure 7: Color image of backscattered energy for a model similar to that of Figure 2 with two 2-mm-diameter malignant tumors separated by 1.5 cm in the depth direction.

(5.0 cm, 3.2 cm), is the dielectric-properties contrast between malignant and normal breast tissue. The low-level energy spatially distributed throughout the image is the heterogeneity of normal breast tissue in the numerical breast phantom. The tumor is clearly detectable as it stands 19 dB above the maximum clutter in a tumor-free model which is defined here as the minimum S/C.

Figures 6(b) and 6(c) repeat the scenario of Figure 6(a) for different tumor locations. The image in Figure 6(b) is based on the backscattered signals computed using a model similar to Figure 2 with the 2-mm-diameter tumor located at a depth of only 1.1 cm. In the model associated with Figure 6(c), the tumor was located 3.0 cm off the center axis at a depth of 2.1 cm. For the case when the modeled tumor is centered at (5.0 cm, 1.1 cm), the minimum S/C is 16 dB, and the peak of the tumor response occurs at (5.0 cm, 1.2 cm). When the modeled tumor is centered at (8.0 cm, 2.1 cm), the minimum S/C is 18 dB, and the peak of the tumor response occurs at (8.1 cm, 2.1 cm).

Figure 7 depicts the beamformer output energy for two adjacent 2-mm-diameter tumors separated by 1.5 cm with the deeper tumor located at a depth of 3.1 cm. Two distinct scattering objects are clearly evident. The response from the 1.6 cm deep tumor has a minimum S/C of 18 dB and the peak occurs at (5.0 cm, 1.6 cm) while the tumor response from the 3.1 cm deep tumor has a minimum S/C of 19 dB and its peak occurs at (5.0 cm, 3.2 cm). This example illustrates the resolving capability of this approach.

In each of the images of Figures 6 and 7, the peak of the tumor response occurs no more than 1 mm from the true center of the tumor. This small discrepancy arises because the reflection occurs at the surface of the tumor, which corresponds to a 1-mm offset from the center

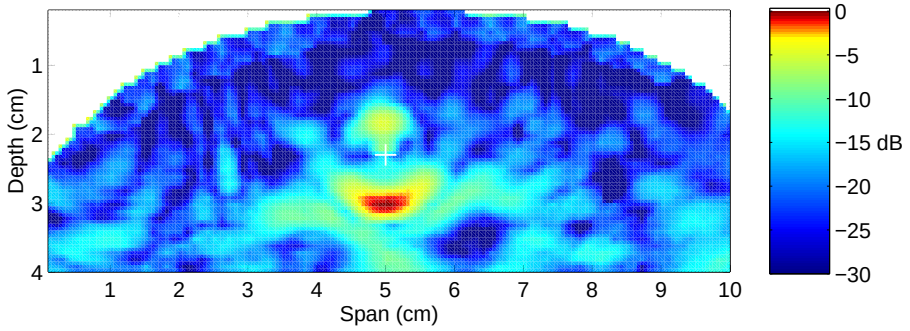

Figure 8: Color image of backscattered energy for a model similar to that of Figure 2 with a 6-mm-diameter malignant tumor centered at (5.0 cm, 2.3 cm).

of the tumor. The beamformer was designed assuming point source scatterers, so it performs well on the relatively small 2 mm tumors considered in these examples. However, the beamformer encounters localization errors when the tumor size in increased.

This effect is clearly illustrated by considering the case of a larger 6-mm-diameter malignant tumor centered at a depth of 2.3 cm. The image of beamformer output energy depicted in Figure 8 shows that the peak of the tumor response appears approximately 1 cm deeper than the physical tumor location. A smaller, but still distinguishable peak occurs at (4.9 cm, 1.8 cm), corresponding to the front surface of the tumor where the initial reflection occurs. The beamformer output for this local peak is shown in Figure 9(a) where the samples that fall in the three-sample window are circled. The window captures a significant portion of the mainlobe, and the peak in energy correctly identifies a scattering surface. Figure 9(b) depicts the beamformer output signal for scan location (5.0 cm, 2.3 cm), the center of the physical tumor. Significant energy is clearly evident, although the short window only captures a small portion of it. An inverted sinc envelope appears in this figure, but the mainlobe falls 5 samples before the selected window. This misalignment is due to the reflection occurring at the tumor surface rather than at the center of the tumor, so the beamformer correctly suppresses energy at this location. Another smaller, but still distinguishable sinc mainlobe lags the window by 6 samples. This peak is a consequence of the reflection from the lower surface of the tumor. Figure 9(c) depicts the beamformer output signal for scan location (5.0 cm, 3.0 cm), the peak-energy location in the image of Figure 8. While the windowing eliminates most of the initial reflection for this deeper scan location, the secondary reflection is preserved, and is actually amplified relative to that in Figure 9(b)

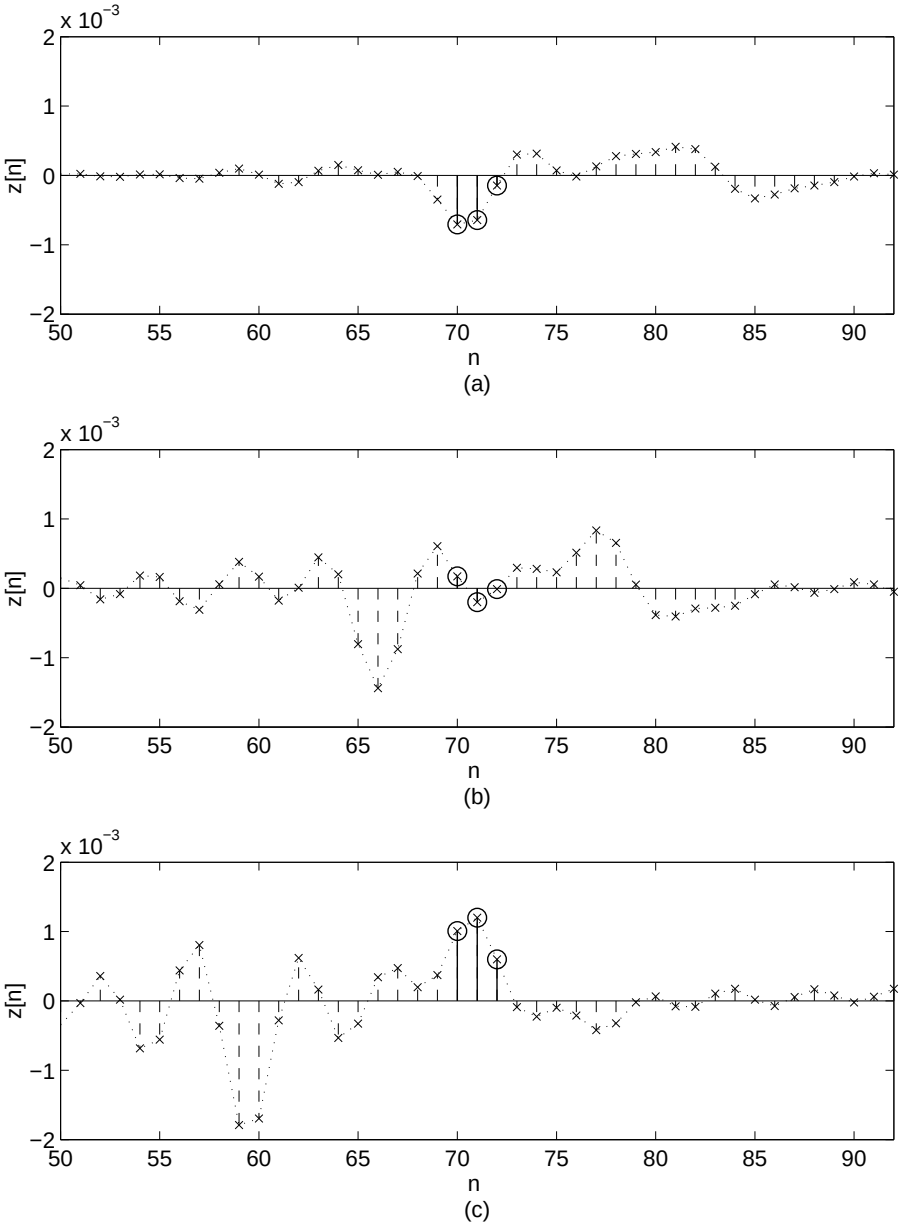

Figure 9: Beamformer output signal for scan location (a) (4.9 cm, 1.9 cm), the location of a local peak of backscatter from a 6-mm-diameter malignant lesion, (b) (5.0 cm, 2.3 cm), the center of the malignant lesion, and (c) (5.0 cm, 3.0 cm), the location of the global peak of tumor energy in Figure 8. The three-sample rectangular window chosen for the case of smaller (2-mm-diameter) lesions is represented by the the circled output signal samples.

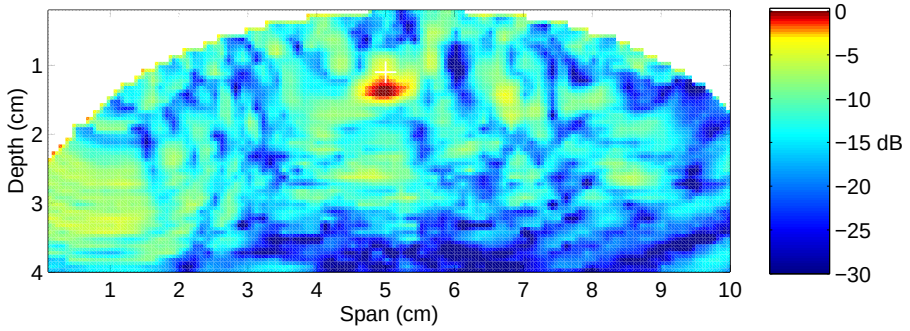

Figure 10: Color image of backscattered energy for a numerical breast phantom with a 2-mm-diameter malignant tumor centered at (5.0 cm, 1.1 cm). The normal-tissue dielectric properties assumed in the numerical breast phantom are increased, thereby introducing a mismatch with that assumed in the beamformer design and reducing the malignant-to-normal contrast from 5:1 in permittivity to 3.2:1.

because of additional gain introduced by the beamformer to compensate for the attenuation associated with a deeper scan location. The three-sample window of Figure 9(c) captures considerably more energy than those in Figures 9(a) and (b). Note that in spite of the relatively large size mismatch between the assumed point-scatterer model and the actual finite-sized tumor, the tumor remains clearly detectable. The minimum S/C is 21 dB, several dB larger than that of the 2 mm tumor. Mismatch simply introduces a location bias.

Images generated by MIST beamforming do not uniquely determine the exact tumor configuration in the breast. This problem of deducing the tumor configuration from the the energy plots does not have a unique solution because different tumor configurations could lead to qualitatively similar energy plots. The image of Figure 8, for example, could conceivably have resulted from a breast model with one small tumor located 1.5 cm above a larger tumor. If, however, one assumes that at most a single tumor is present then the image does provide insight into tumor properties, such as size.

All of the previous results were obtained using beamformers that were designed for the actual average dielectric properties of the normal breast tissue present in the model. In practice, these properties will vary from patient to patient within a certain margin, and exact normal breast tissue properties will be unknown. The robustness of our frequency-domain design with respect to potential mismatch between the assumed and the actual dielectric properties averages is demonstrated by applying it to backscattered signals obtained from a breast model with average permittivity of normal breast tissue that is

60% higher than that assumed in the beamformer design. This represents an extreme case of mismatch – one which exceeds that expected in practice. Also note that this case demonstrates the potential of our approach for detecting malignant tumors that exhibit a smaller contrast with normal breast tissue. In this example, the contrast in permittivity is 3.2:1 instead of the previous 5:1 contrast. The 2-mm-diameter malignant tumor is located at (5.0 cm, 1.1 cm) in the model, permitting a direct comparison with the results of Figure 6(b). Figure 10 shows the output energy image. Despite the mismatch and the decreased malignant-to-normal contrast, the 2-mm malignant tumor is still clearly detectable with a minimum S/C of 10 dB.

4 Conclusions

We have proposed and demonstrated a frequency-domain approach to designing a MIST beamformer for detecting millimeter-sized malignant tumors in the breast. The frequency-domain MIST beamformer design minimizes a penalized least-squares problem that compensates for frequency-dependent propagation effects and proves to be computationally simpler than our time-domain MIST beamformer design. Furthermore, the frequency-domain MIST beamformer is suitable for use with widely available narrowband signal generating instruments, effectively lifting the burden of generating and radiating UWB pulses. Simulation results show that this method achieves tightly focused, high-energy peaks at image locations that consistently correspond to surfaces of malignant tumors in the breast. We have shown that this method exhibits robustness to several potential challenges associated with imaging the inherently heterogeneous breast. Due to the enhanced synthetic-focusing capabilities of the frequency-domain MIST beamforming approach, the imaged backscatter from a 2-mm-diameter tumor stands out significantly above the natural variations in the fibroglandular and adipose composition of the breast. Small lesions can be detected with high sensitivity regardless of location in the breast. The spatial selectivity of MIST beamforming also overcomes the challenge of detecting, localizing, and resolving multiple or multi-focal lesions. Small tumors are successfully detected even when a significant mismatch exists between the average and normal-breast-tissue dielectric properties assumed in the beamformer design and a priori knowledge of the actual average dielectric properties of normal breast tissue does not appear to be required for detection. Although the design constraint used in the penalized least-squares problem statement yielded a high S/C, the constraint choice has not been optimized and

further consideration of the constraint may lead to improved S/C performance.

Acknowledgment

This work was supported by The Whitaker Foundation Biomedical Engineering Research Grant RG-99-0004, the Department of Defense Breast Cancer Research Program under award DAMD17-02-1-0625, and the University of Wisconsin Graduate Engineering Research Scholars program. Computing resources were provided in part by Cray, Inc.

References

[1] *Mammography and Beyond: Developing Techniques for the Early Detection of Breast Cancer*, Institute of Medicine, National Academy Press, Washington D.C., 2000.

[2] Surowiec, A. J., S. S. Stuchly, J. R. Barr, and A. Swarup, "Dielectric properties of breast carcinoma and the surrounding tissues," *IEEE Trans. Biomed. Eng.*, vol. 35, pp. 257–263, Apr. 1988.

[3] Joines, W. T., Y. Z. Dhenxing, and R. L. Jirtle, "The measured electrical properties of normal and malignant human tissues from 50 to 900 MHz," *Med. Phys.*, vol. 21, pp. 547–550, Apr. 1994.

[4] Chaudhary, S. S., R. K. Mishra, A. Swarup, and J. M. Thomas, "Dielectric properties of normal and malignant human breast tissues at radiowave and microwave frequencies," *Indian J. Biochem. and Biophys.*, vol. 21, pp. 76–79, Feb. 1984.

[5] Hagness, S. C., X. Li, K. M. Leininger, J. H. Booske, and M. Okoniewski, "Dielectric characterization of human breast tissue and breast cancer detection algorithms for confocal microwave imaging," in *Microwaves: Theory and Applications in Materials Processing V*, D. E. Clark, J. G. P. Binner, and D. A. Lewis, eds., Westerville, OH: The American Ceramic Society, 2001.

[6] Hagness, S. C., A. Taflove, and J. E. Bridges, "Two-dimensional FDTD analysis of a pulsed microwave confocal system for breast cancer detection: Fixed-focus and antenna-array sensors," *IEEE Trans. Biomed. Eng.*, vol. 45, no. 12, pp. 1470–1479, Dec. 1998.

[7] Foster, K. R. and H. P. Schwan, "Dielectric properties of tissues and biological materials: A critical review," *Critical Reviews for Biomedical Engineering*, vol. 17, pp. 25–104, 1989.

[8] Souvorov, A. E., A. E. Bulyshev, S. Y. Semenov, R. H. Svenson, and G. P. Tatsis, "Two-dimensional computer analysis of a microwave flat antenna array for breast cancer tomography," *IEEE Trans. Microwave Theory Tech.*, vol. 48, no. 8, pp. 1413–1415, Aug. 2000.

[9] Bulyshev, A. E., S. Y. Semenov, A. E. Souvorov, R. H. Svenson, A. G. Nazarov, Y. E. Sizov, and G. P. Tatsis, "Computational modeling of three-dimensional microwave tomography of breast cancer," *IEEE Trans. Biomed. Eng.*, vol. 48, no. 9, pp. 1053–1056, Sept. 2001.

[10] Meaney, P. M. and K. D. Paulsen, "Nonactive antenna compensation for fixed-array microwave imaging: Part II–Imaging results," *IEEE Trans. Med. Imag.*, vol. 18, no. 6, pp. 508–518, June 1999.

[11] Meaney, P. M., M. W. Fanning, D. Li, S. P. Poplack, and K. D. Paulsen, "A clinical prototype for active microwave imaging of the breast," *IEEE Trans. Microwave Theory Tech.*, vol. 48, no. 11, pp. 1841–1853, Nov. 2000.

[12] Bond, E. J., X. Li, S. C. Hagness, and B. Van Veen, "Microwave Imaging via Space-Time Beamforming for Early Detection of Breast Cancer," submitted to *IEEE Trans. Antennas and Propagat.*

[13] Hagness, S., A. Taflove, and J. E. Bridges, "Three-dimensional FDTD analysis of a pulsed microwave confocal system for breast cancer detection: Design of an antenna-array element," *IEEE Trans. Antennas and Propagat.*, vol. 47, no. 5, pp. 783–791, May 1999.

[14] Fear, E. C., and M. A. Stuchly, "Microwave detection of breast cancer," *IEEE Trans. Microwave Theory Tech.*, vol. 48, no. 11, pp. 1854–1863, Nov. 2000.

[15] Li, X. and S. C. Hagness, "A confocal microwave imaging algorithm for breast cancer detection," *IEEE Microwave and Wireless Components Lett.*, vol. 11, no. 3, pp. 130–132, Mar. 2001.

[16] Cox, H., "Resolving power and sensitivity to mismatch of optimum array processors," *Jour. Acoust. Soc. Amer.*, vol. 54, no. 3, pp. 771-785, 1973.

[17] Cox, H., R. M. Zeskind, and M. M. Owen, "Robust adaptive beamforming," *IEEE Trans. on ASSP*, vol ASSP-35, pp. 1365-1375, Oct. 1987.

[18] Taflove, A. and S. Hagness, *Computational Electrodynamics: The Finite-Difference Time-Domain Method, 2nd ed.*, Artech House, Boston, MA, 2000.

[19] Haykin, S., *Adaptive Filter Theory*, Prentice-Hall, New Jersey, 3rd ed., 1996.

[20] Van Veen, B. and K. Buckley, "Beamforming: A versatile approach to spatial filtering," *IEEE ASSP Magazine*, vol. 5, pp. 4–24, April 1988.

[21] Van Veen, B., "Minimum variance beamforming," in *Adaptive Radar Detection and Estimation*, S. Haykin and A. Steinhardt, eds., Chapter 4, pp. 161–236. John Wiley and Sons, New York, 1992.

[22] Balanis, C., *Advanced Engineering Electromagnetics*, John Wiley and Sons, New York, 1989.

Shakti Davis was born in Austin, Texas, on July 27, 1976. She received the B.S. degree in Electrical Engineering from New Mexico Sate University in December 1999 and is currently pursuing her M.S. degree in the Department of Electrical and Computer Engineering at the University of Wisconsin-Madison. Her research interests include microwave imaging and wireless communications. Ms. Davis was the recipient of a Graduate Engineering Research Scholars Fellowship from the UW-Madison.

Essex J. Bond was born in Milwaukee, Wisconsin, on November 18, 1977. He received the B.S. degree from the Milwaukee School of Engineering in May 1999 and the M.S. degree from the University of Wisconsin-Madison in August 2001, both in Electrical Engineering. He is currently pursuing his Ph.D. degree in the Department of Electrical and Computer Engineering at the University of Wisconsin-Madison. His research interests include statistical signal processing and microwave imaging. Mr. Bond was the recipient of a Graduate Engineering Research Scholars Fellowship from the UW-Madison.

Xu Li was born in Beijing, China, on May 13, 1975. She received the B.S. degree in Biomedical Engineering from Tsinghua University, Beijing, China and the M.S. degree in Biomedical Engineering from the University of Wisconsin-Madison, WI in 1998 and 2000, respectively. Currently she is pursuing her Ph.D degree in the Department of Electrical and Computer Engineering at the University of Wisconsin-Madison. Her research interests include microwave imaging, computational electromagnetics, and ultrawideband antennas. Ms. Li was

the recipient of a Wisconsin Alumni Research Foundation Graduate Fellowship from the UW-Madison in 1998. She is currently a student member of the IEEE.

Susan C. Hagness received the B.S. degree with highest honors and the Ph.D. degree in electrical engineering from Northwestern University in 1993 and 1998, respectively. Since August of 1998, she has been with the University of Wisconsin-Madison, where she is currently an assistant professor in the Department of Electrical and Computer Engineering and a faculty affiliate of the Department of Biomedical Engineering. In 2000, Dr. Hagness received the Presidential Early Career Award for Scientists and Engineers (PECASE) from the White House. She is also the recipient of the UW ECE Holdridge Excellence in Teaching Award (2000). In 2002, she was named one of the 100 top young innovators in science and engineering by MIT's Technology Review magazine. She co-authored Computational Electrodynamics: The Finite-Difference Time-Domain Method, 2nd. ed. (Artech House, 2000) with Allen Taflove, and is currently serving as an associate editor for the IEEE Antennas and Wireless Propagation Letters.

Barry D. Van Veen received the B.S. degree from Michigan Technological University in 1983 and the Ph.D. degree from the University of Colorado in 1986, both in electrical engineering. Since August of 1987 he has been with the Department of Electrical and Computer Engineering at the University of Wisconsin-Madison and currently holds the rank of Professor. Dr. Van Veen was a recipient of a 1989 Presidential Young Investigator Award from the National Science Foundation and a 1990 IEEE Signal Processing Society Paper Award. He served as an associate editor for the IEEE Transactions on Signal Processing and on the IEEE Signal Processing Society's Technical Committee on Statistical Signal and Array Processing from 1991 through 1997 and is currently a member of the Sensor Array and Multichannel Technical Committee. He is a Fellow of the IEEE and received the Holdridge Teaching Excellence Award from the ECE Department at the University of Wisconsin in 1997. He coauthored "Signals and Systems," (Wiley 1999) with Simon Haykin.